

The 21 centimeter emission from the reionization epoch: extended and point source foregrounds

Tiziana Di Matteo, Benedetta Ciardi and Francesco Miniati

Max-Planck-Institut für Astrophysik, Karl-Schwarzschild-Straße 1, 85748 Garching, Germany

arXiv:astro-ph/0402322v1 13 Feb 2004

September 2003

ABSTRACT

Fluctuations in the redshifted 21 centimeter emission from neutral hydrogen probe the epoch of reionization. We examine the observability of this signal and the impact of extragalactic foreground radio sources (both extended and point-like). We use cosmological simulations to predict the angular correlation functions of intensity fluctuations due to unresolved radio galaxies, cluster radio halos and relics and free-free emission from the interstellar and intergalactic medium at the frequencies and angular scales relevant for the proposed 21cm tomography. In accord with previous findings, the brightness temperature fluctuations due to foreground sources are much larger than those from the primary 21cm signal at all scales. In particular, diffuse cluster radio emission, which has been previously neglected, provides the most significant foreground contamination. However, we show that the contribution to the angular fluctuations at scales $\theta \gtrsim 1$ arcmin is dominated by the spatial clustering of bright foreground sources. This excess can be removed if sources above flux levels $S \gtrsim 0.1$ mJy (out to redshifts of $z \sim 1$ and $z \sim 2$ for diffuse and point sources respectively) are detected and removed. Hence, efficient source removal may be sufficient to allow the detection of angular fluctuations in the 21cm emission free of extragalactic foregrounds at $\theta \gtrsim 1$ arcmin. In addition, the removal of sources above $S = 0.1$ mJy also reduces the foreground fluctuations to roughly the same level as the 21cm signal at scales $\theta \lesssim 1$ arcmin. This should allow the subtraction of the foreground components in frequency space, making it possible to observe in detail the topology and history of reionization.

Key words: cosmology:theory – intergalactic medium – diffuse radiation – galaxies: active – radio continuum:general

1 INTRODUCTION

In the past few years a quantitative study of the high-redshift intergalactic medium (IGM) and its reionization history has finally been made possible by the discovery of quasars at $z > 5.8$ (e.g. Fan et al. 2001, 2003). In particular, the detection of a Gunn-Peterson trough (Gunn & Peterson 1965) in the Keck (Becker et al. 2001) and VLT (Pentericci et al. 2002) spectra of the Sloan Digital Sky Survey quasar SDSS 1030-0524 at $z = 6.28$ and in the Keck spectrum of SDSS 1148+5251 at $z = 6.37$ (White et al. 2003), has been interpreted as the signature of the trailing edge of the cosmic reionization epoch. The recent analysis of the first year of data from the Wilkinson Microwave Anisotropy Probe (WMAP) satellite on the temperature and polarization anisotropies of the cosmic microwave background (CMB), infers a mean optical depth to Thomson scattering $\tau_e \sim 0.17$, suggesting that the universe was reionized at

higher redshift (Kogut et al. 2003; Spergel et al. 2003). Physically, the CMB and the Gunn-Peterson trough probe two different stages of reionization, the former being sensitive to the initial phase, when free electrons appear, the latter to the residual neutral hydrogen in the latest stages of reionization. None of the two methods though is able to constrain the exact ionization level or the details of the reionization history. For this reason, an alternative way to probe the high-redshift IGM is required.

An optimal experiment for probing the various stages of reionization is the proposed 21cm tomography. It has indeed been shown that neutral hydrogen in the intergalactic medium (IGM) and gravitationally collapsed systems should be directly detectable in emission or absorption against the cosmic microwave background radiation (CMB) at frequencies corresponding to the 21cm line (e.g.;Field 1958, 1959; Scott & Rees 1990; Kumar et al. 1995). In principle it will be possible to carry out such an experiment with planned high

sensitivity radio telescopes such as the PrimeVAL Structure Telescope (PAST)^{*}, the Square Kilometer Array (SKA)[†] and the LOw Frequency ARray (LOFAR)[‡]. The 21cm spectral features will display redshift dependent angular structure due to evolving inhomogeneities in the gas density field, hydrogen ionized fraction, and spin temperature. Several different signatures have been investigated in the recent literature: the fluctuations in the 21cm line emission induced both by the inhomogeneities in the gas density and in the ionized hydrogen fraction (Madau, Meiksin & Rees 1997; Tozzi et al. 2000; Ciardi & Madau 2003, hereafter CM; Furlanetto, Sokasian & Hernquist 2004) and by ‘minihalos’ with virial temperatures below 10^4 K (Iliev et al. 2002, 2003); the global feature (‘reionization step’) in the continuum spectrum of the radio sky that may mark the abrupt overlapping phase of individual intergalactic HII regions (Shaver et al. 1999); and the 21cm narrow lines generated in absorption against very high redshift radio sources by the neutral IGM (Carilli, Gnedin & Owen 2002) and by intervening minihalos and protogalactic disks (Furlanetto & Loeb 2002).

While the 21cm tomography proposes to map the topology of the reionization process and constrain the nature of the ionizing sources, it remains a challenging project due to foreground contamination from unresolved extragalactic radio sources (Di Matteo et al. 2002), free-free emission from the same halos that reionize the universe (Oh & Mack 2003) and the Galactic free-free and synchrotron emission (Shaver et al. 1999). Because the proposed experiments will be carried out in frequency space as well as angle, recent work has discussed the possibility of removing the foreground power spectrum components by comparing maps closely spaced in frequency (Zaldarriaga, Furlanetto & Hernquist 2004; Gnedin & Shaver 2004). The proposed subtraction is nonetheless demanding as the foreground fluctuations overwhelm the primary 21cm signal by up to three orders of magnitude. In particular, it will require knowing in detail the spectral behavior and possible spectral variations of each of the contaminants and their associated angular power spectra.

In this paper we employ computer simulations of a Λ CDM universe to evaluate the foreground brightness temperature fluctuations due to extragalactic sources that contaminate the 21cm tomography. In particular, we model the free-free emission from ionizing sources self-consistently with a viable reionization scenario and with the associated 21cm IGM emission (as described in CM). Using the same simulations we adopt simple but physically motivated prescriptions to model the radio galaxy population; the model successfully reproduces both the observed luminosity function (at 1.4GHz) and the two point correlation function of the observed radio sources. Finally, we use a separate simulation (of the same Λ CDM universe) that, in addition to dark matter and baryonic gas, follows the evolution of magnetic fields and cosmic rays, to estimate the foreground signals due to extended radio sources such as cluster radio relics and radio halos, which had not been considered in previous work.

^{*} <http://astrophysics.phys.cmu.edu>

[†] <http://www.nfra.nl/skai>

[‡] <http://www.astron.nl/lofar>

We shall show that the detailed information on the spatial and redshift distribution of the contaminant sources is crucial for determining the correct brightness temperature fluctuations due to the unresolved extragalactic foregrounds on the angular scales where the primary 21cm signal is expected to peak. By modeling the foregrounds within the cosmological simulations we are able to study and map the variation of the angular clustering signal as a function of the flux cut above which foreground sources will be detected (and hence will not contribute to the unresolved fluctuating signal). In particular, we will show that the angular power spectra of unresolved foreground contaminants become significantly suppressed at scales $\theta \gtrsim 1$ arcmin when sources above flux levels of a fraction of mJy are removed.

The structure of the paper is as follows. In Section 2 we describe the numerical simulations adopted to model the physical processes producing the extragalactic backgrounds. In Section 3 we briefly outline the origin of the 21cm emission line from the diffuse IGM used in CM, while in Section 4 we show the total comoving emissivities and spatial correlation functions for the extragalactic foregrounds modeled within the simulations. In Sections 5, and 6 we calculate the contribution to the brightness temperature fluctuations to the clustering of the different foregrounds and finally, in Section 7 we give our conclusions.

2 NUMERICAL SIMULATIONS

In this Section we briefly describe the numerical simulations adopted to model the various emission processes considered in this paper and refer to Ciardi, Stoehr & White (2003, hereafter CSW), Ciardi, Ferrara & White, (2003, hereafter CWF) and Miniati (2002) for further details.

All simulations assume a Λ CDM “concordance” cosmology with $\Omega_m=0.3$, $\Omega_\Lambda=0.7$, $h=0.7$, $\Omega_b=0.04$, $n=1$ and $\sigma_8=0.9$. These parameters are within the WMAP experimental error bars (Spergel et al. 2003).

The simulations used to model the foregrounds produced by radio galaxies and free-free emission from HII regions are based on the N-body code **GADGET** (Springel, Yoshida & White 2001). A “re-simulation” technique (Springel et al. 2001, hereafter SWTK) was employed in order to follow at high resolution the dark matter distribution within an approximately spherical region with a diameter of about $50h^{-1}$ Mpc within a cosmological volume of $479 h^{-1}$ Mpc on a side (Yoshida, Sheth & Diaferio 2001). The location and mass of dark matter halos was determined with a friends-of-friends algorithm. Gravitationally bound substructures were identified within the halos with the algorithm **SUBFIND** (SWTK) and were used to build the merging tree for halos and subhalos following the prescription of SWTK. The smallest resolved halos have masses of $M \simeq 10^9 M_\odot$ (the particle mass is $M_p = 1.7 \times 10^8 h^{-1} M_\odot$). The galaxy population was modeled via the semi-analytic technique of Kauffmann et al. (1999) and implemented in the way described by SWTK. We obtain in this way, a catalogue of galaxies for each of the simulation outputs, containing for each galaxy, among other quantities, its position, mass and star formation rate. We used the galaxies within the $50h^{-1}$ Mpc region, coupled with the prescriptions described in Section 4, to model the redshift distribution and

luminosity function of radio galaxy population and the free-free emission from the interstellar medium (ISM).

Within the high resolution spherical subregion, a cube of comoving side $L = 20h^{-1}$ Mpc was used to study the details of the reionization process, using the radiative transfer code **CRASH** (Ciardi et al. 2001; Maselli, Ferrara & Ciardi 2003) to model the propagation of ionizing photons into the IGM. Several sets of radiative transfer simulations were run in CSW and CFW, with different choices for the galaxy emission properties. The ones used here are those labeled S5 ('late' reionization case) and L20 ('early' reionization case) which employ an emission spectrum typical of Pop III stars, a Salpeter Initial Mass Function (IMF) and an escape fraction of ionizing photons $f_{esc} = 5\%$ and a Larson IMF with $f_{esc} = 20\%$ respectively. For details and discussion on the choice of parameters we refer to CSW and CFWS. These simulations provide the redshift evolution and the spatial distribution of ionized IGM and have been used to model the free-free emission from the IGM.

For the diffuse radio emission associated with cluster radio halos and relics we have used a different simulation of the same cosmological model, in which in addition to dark matter and baryonic gas, magnetic fields and cosmic-rays (CR) were also followed. In the simulation, the cosmological code of Ryu et al. (1993) is used in combination with the cosmic-ray code **COSMOCR** fully described in Miniati (2001, 2002). Basically, during the simulation large scale structure shocks are identified and their jump conditions computed (Miniati et al. 2000). A fraction of the particles crossing the shock is assumed to be injected in the diffusive shock acceleration mechanism, and thereafter accelerated to a power-law spectrum in momentum space. The log-slope of the distribution is determined by the shock Mach number (\mathcal{M}) in accord with the test particle limit (e.g. Bell 1978). The fraction of injected CR protons is computed according to a variant of the thermal leakage prescription (e.g. Kang & Jones 1995); for practical purposes it amounts to about several $\times 10^{-5}$. The fraction of injected CR electrons is assumed to be 100 times smaller than that (to be roughly consistent with measurements of this parameter from supernova remnants observations and with EGRET γ -ray upper limits at 100 MeV for nearby clusters of galaxies; Miniati 2002). Both populations of shock accelerated CRs (*primaries*) are then passively advected with the baryonic flow. In addition, we follow the evolution of their momentum spectrum by accounting for all relevant mechanisms of energy loss, such as Coulomb collisions, adiabatic, bremsstrahlung, synchrotron and inverse Compton losses for the electrons; and Coulomb and inelastic p-p collisions for the CR protons. As a byproduct of inelastic p-p collisions *secondary* e^\pm are also generated. Thus with the same prescription as for the primary electrons, the simulation follows the evolution of secondaries as well. The simulation employs a computational box of $50 h^{-1}$ Mpc on a side, a grid of 512^3 cells and 256^3 dark matter particles. With the cosmological parameters described at the beginning of this Section, each numerical cell measures about $100 h^{-1}$ kpc (comoving) and each dark matter particle corresponds to $2 \times 10^9 h^{-1} M_\odot$. Finally, momentum space for the CR components is subdivided into a few equidistant logarithmic momentum bins as detailed in Miniati (2002).

3 THE 21CM RADIATION FROM THE INTERGALACTIC MEDIUM

The 21 cm hyperfine transition of neutral hydrogen in the IGM provides a powerful probe for studies of the history of reionization. The physics of this transition has been well studied in the cosmological context, initially using linear theory (Scott & Rees 1990; Kumar et al. 1995; Madau, Meiksin & Rees 1997; Tozzi et al. 2000) and more recently using numerical simulations of reionization (CM; Furlanetto, Sokasian & Hernquist 2004). In this work we use the results from the simulations by CM (which we refer the reader to for further details) to compare the foreground to the intrinsic 21 cm signal.

The emission in the 21cm line is governed by the spin temperature, T_S . In the presence of the CMB radiation, T_S quickly reaches thermal equilibrium with the CMB temperature, T_{CMB} , and a mechanism is required that decouples the two temperatures. While the spin-exchange collisions between hydrogen atoms proceed at a rate that is too small for realistic IGM densities, Ly α pumping contributes significantly by mixing the hyperfine levels of neutral hydrogen in its ground state via intermediate transitions to the $2p$ state. When the first objects form, Ly α pumping will efficiently decouple T_S from T_{CMB} if $J_\alpha > 10^{-21} \text{ ergs cm}^{-2} \text{ s}^{-1} \text{ Hz}^{-1} \text{ sr}^{-1}$. CM find that the expected diffuse flux of Ly α photons produced by the same sources responsible for the IGM reionization, satisfies the above requirement during the 'grey age', from redshift ~ 20 to the time of complete reionization. As the IGM can be easily preheated by primordial sources of radiation (e.g. Madau, Meiksin & Rees 1997; Chen & Miralda-Escudé 2003), the universe will, most likely, be observable in 21cm emission at a level that is independent of the exact value of T_S . Variations in the density of neutral hydrogen (due to either inhomogeneities in the gas density or different ionized fraction) should appear as fluctuations of the sky brightness of this transition (e.g. as a brightness temperature increment with respect to the CMB at an observed frequency ν corresponding to a redshift $1+z = \nu_o/\nu$, given by $\delta T(\nu) = (T_S - T_{CMB})\tau/(1+z)$ where τ is the optical depth of a patch of IGM in the hyperfine transition; see e.g. Field 1959). In principle, high resolution observations of the 21cm line transition in both frequency (hence redshift) and angle should provide a detailed map of reionization.

CM studied the evolution of brightness temperature fluctuations in both the 'late' and 'early' reionization models (the S5 and the L20 models respectively, described in Section 2). The S5 model predicts a peak in the amplitude of the surface brightness fluctuations at $\nu \sim 115$ MHz whereas in the L20 the peak occurs at $\nu \sim 90$ MHz. The overall amplitude of the signal at its peak, in both models is $\langle \delta T_{rms}^2 \rangle^{1/2} \sim 10 - 20$ mK at angular scales $\theta \sim 5$ arcmin (see CM for details). When comparing the foreground fluctuations to that of the primary redshifted 21cm we will mainly use the S5 model where the peak in the 21cm signal occurs at frequencies which will most easily be probed by the upcoming telescopes (this choice will not affect any of the analysis performed here). We will examine the frequency and angular dependence of 21cm signal and foregrounds in the Conclusions.

4 EXTRAGALACTIC FOREGROUND SOURCES

In this Section we describe the properties of the sources responsible for the extragalactic foreground signal. In particular, we describe how we model their redshift distribution to calculate their spatial correlation functions and luminosity functions from the simulations. We will show that our models are able to reproduce reasonably well the observed populations and hence should provide us with a physically grounded framework for examining the contribution to the temperature fluctuations due to unresolved sources.

We consider two main classes of sources. (a) Point sources: (i) radio galaxies/AGN which produce synchrotron emission in their nuclei; (ii) HII regions inside ionizing halos which produce free-free emission. (b) Extended sources: (i) HII regions in the IGM which produce free-free emission; (ii) cluster radio halos and (iii) cluster radio relics, which both produce synchrotron emission. As we shall see in Section 5, radio galaxies, cluster radio halos and relics appear to provide the most significant contribution to the sky brightness temperature fluctuations at angular scales of a few arcmin.

4.1 Radio Galaxies

In this Section we describe the simple scheme we have implemented in the simulations to reproduce the properties of the observed radio galaxy population. The physical processes that determine the amount of radio power from active galactic nuclei (AGN) are poorly understood. However, the radio power in AGN must be linked to the presence of the supermassive black hole in center of galaxies and to the accretion of gas onto it. Several groups have discussed the link between cosmological evolution of AGN and the formation history of galaxies using semianalytic models of galaxy formation (see e.g.; Monaco et al. 2000; Kauffmann & Haehnelt 2000; Cavaliere & Vittorini 2000; Wyithe & Loeb 2002; Volonteri, Haardt & Madau 2003; Haiman, Ciotti & Ostriker 2004 and references therein) and recently using cosmological hydrodynamic simulations (Di Matteo et al. 2003ab). Such models have been shown to successfully reproduce the B-band luminosity functions of QSOs and in some cases the X-ray luminosity functions as well. Here we make the hypothesis that the radio activity is also linked to the growth and accretion of gas onto black holes and hence to the activity seen in the optical and X-ray bands. In particular, we use a prescription similar to that adopted in previous works to couple the cosmological simulations described in Section 2 with a simple scheme for the radio population. Note that we shall not attempt to build a detailed model for the radio galaxy population but merely reproduce its main observed properties such as the luminosity functions and their angular clustering.

The fraction of gas accreted by the central black hole in galaxies must be related to the observed correlation between stellar velocity dispersion and black hole mass (Ferrarese & Merritt 2000; Gebhardt et al. 2000). Using the most recently revised set of black hole mass and velocity dispersion measurements (Tremaine et al. 2002), the $M_{\text{BH}} - \sigma$ relation gives:

$$M_{\text{BH}} = (1.5 \pm 0.2) \times 10^8 M_{\odot} \left(\frac{\sigma}{200 \text{ km s}^{-1}} \right)^4, \quad (1)$$

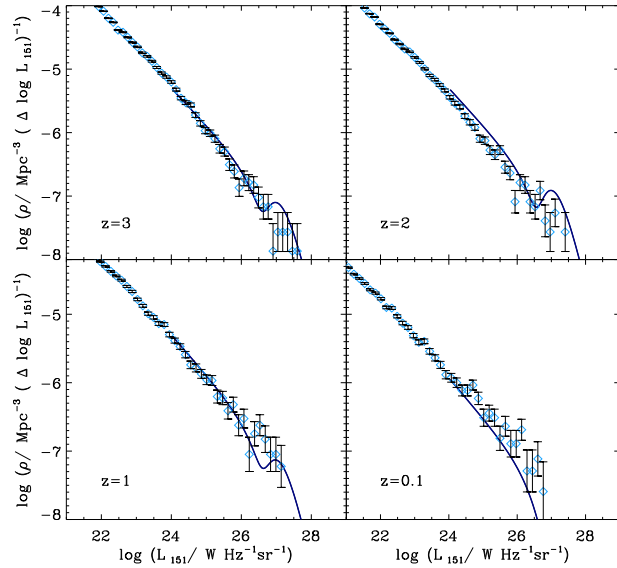


Figure 1. The radio luminosity function at 150 MHz in the simulations (diamond symbols) plotted with Poisson error bars compared to the analytical fits (solid lines) of the observed luminosity functions from Willott et al. (2001) from the 3CRR, 6CE and 7CRS samples.

where σ is the velocity dispersion of stars in the bulge. Ferrarese (2002) and Baes et al. (2003) find that the stellar velocity dispersion measured in galaxies is strictly correlated with the asymptotic value of the circular velocity, V_c :

$$\log V_c = 0.9 \log \sigma + 0.3. \quad (2)$$

A $V_c - \sigma$ relation consistent with the observations has also been measured from the simulations (Eq. 8; Di Matteo et al. 2003a). In order to avoid introducing any details on how gas cooling, star formation and feedback is linked to black hole fueling, we simply combine the previous two relations to find the mass accreted by a supermassive black hole. We assume this mass to be accreted at the Eddington rate after a timescale $t_Q \sim t_{\text{dyn}} \sim 0.1 r_{\text{vir}}/V_c$, where t_{dyn} is the dynamical timescale estimated at a tenth of the virial radius, r_{vir} . All galaxies are assumed to undergo active phases with a duty cycle given simply by $f_Q = t_Q/t_{H(z)}$ where $t_{H(z)}$ is the Hubble time at redshift z . This fraction gives us the expected number density of active black holes at a given redshift. We then use the empirical relation found by Merloni, Heinz & Di Matteo (2003) and Falcke, Koerding & Markoff (2003) to infer the radio luminosity. For each galaxy of a given nuclear X-ray luminosity and black hole mass, the relation gives,

$$\log L_{\text{R}}^{\text{RG}} = 0.6 \log L_{\text{X}} + 0.8 \log M_{\text{BH}} + 7, \quad (3)$$

where L_{X} is the X-ray luminosity in the 2 – 10 keV band, which is related to the bolometric luminosity with a correction $L_{\text{X}} \sim 0.01 L_{\text{bol}}$ (Elvis et al. 1994; Elvis, Risaliti & Zamorani 2002). In Eq. 3, L_{R}^{RG} is the radio luminosity at 5 GHz. In Fig. 1, we show the radio luminosity functions at 150 MHz and for $z = 3, 2, 1, 0.1$ obtained from the simulations (diamond symbols) using L_{R}^{RG} in Eq. 3 and assuming a power law spectrum which gives us the luminosity of the radio sources at a given frequency simply as $L_{\nu}^{\text{RG}} \propto \nu^{-\alpha}$

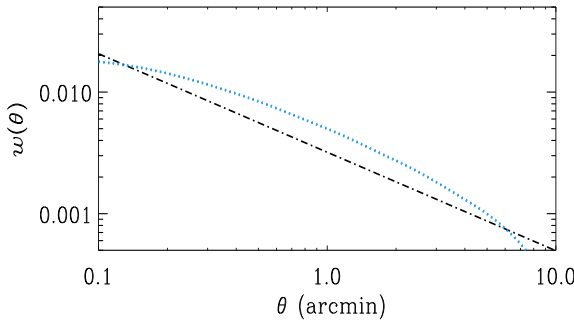


Figure 2. Angular correlation function of the simulated radio galaxies (dotted line) compared to a power law with slope (in log-log) $1 - \gamma = 0.8$ and amplitude $A = 2 \times 10^{-3}$. The amplitude and shape of the angular correlation function is consistent with the one inferred from observations of faint radio galaxies in the NVSS and FIRST surveys.

with spectral index $\alpha = 0.8$. The results from the simulations are compared with the luminosity functions at 150 MHz most recently measured by Willott et al. (2001) from the 3CRR, 6CE and 7CRS radio surveys (shown with the solid lines)[§] consistent with the models of Dunlop & Peacock (1990). Note that because of the limited size of our simulation box our luminosity function does include a small number of bright (very massive) objects.

By projecting the maps from the simulations we also calculate the angular correlation function, $w(\theta)$ of the radio galaxy population (shown in Fig. 2) defined as,

$$w(\theta) = \langle \delta(\underline{\phi})\delta(\underline{\phi} + \underline{\theta}) \rangle, \quad (4)$$

where $\underline{\phi}$, $\underline{\theta}$ are angular coordinates, $\theta = |\underline{\theta}|$, and $\delta(\underline{\phi}) = [n(\underline{\phi})/\langle n \rangle] - 1$, where $n(\underline{\phi})$ is number density of galaxies per unit solid angle at angular position $\underline{\phi}$. Our estimate of $w(\theta)$, is calculated from the Limber projection of the spatial correlation function of radio galaxies. The details of this calculation are described in Section 5.4. The dash-dotted line in Fig. 2 shows the conventional power-law form $w(\theta) = A\theta^{1-\gamma}$ (e.g. Peebles 1993) where $1 - \gamma = 0.8$ and $A = 2 \times 10^{-3}$. The amplitude A and the shape of the angular correlation function are fully consistent with the values measured for cosmological clustering of the 1.4 GHz NVSS and FIRST radio surveys in the milliJankys and sub-milliJankys populations which show that A_{obs} is fairly constant at these flux limits and $A_{obs} \sim 1 - 4 \times 10^{-3}$ for $1 - \gamma = 0.8$ (Magliocchetti et al. 1998; Richards 2000; Overzier et al. 2003; Willman et al. 2003). In summary, our simple model of the radio galaxy population broadly reproduces the observed luminosity functions and angular clustering of the faint radio source population.

[§] Note that the bumps seen in the fit to the luminosity function of Willott et al. (2001) are probably not real and may be due to restricted number of parameters in their model. The important feature is a break in the high and low luminosity populations with the low luminosity population disappearing at low redshifts.

4.2 Free-Free Emission from HII Regions - ISM and IGM

In this Section we will discuss the free-free emission from ionized regions, both in the ISM and IGM and how they are derived from the simulations. The free-free luminosity at frequency ν from an ionized region of proper volume V_{ion} is given by $L_{\nu}^{ff} = \epsilon_{\nu} V_{ion}$, where ϵ_{ν} is the free-free emissivity for an hydrogen plasma at temperature T and electron number density n_e , $\epsilon_{\nu} = 3.2 \times 10^{-39} n_e^2 (T/10^4 \text{ K})^{-0.35} \text{ erg s}^{-1} \text{ cm}^{-3} \text{ Hz}^{-1}$ (e.g. Rybicki & Lightman 1979; Oh 1999).

The free-free luminosity associated with the ionized ISM of a galaxy can be estimated by taking the free-free emissivity to be directly proportional to the recombination rate. In particular, following the same prescription used by Oh (1999), we can write the recombination rate as:

$$\dot{N}_{rec} = \alpha_B n_e^2 V_{ion} \approx (1 - f_{esc}) \dot{N}_{ion}, \quad (5)$$

where α_B is the case B recombination coefficient (appropriate for the densities of interest here), f_{esc} is the escape fraction of ionizing photons and \dot{N}_{ion} is the ionization rate of the galaxy. Using the above equation to estimate the product $n_e^2 V_{ion}$ and assuming that the temperature of the ionized regions is $T \sim 10^4 \text{ K}$, it is straightforward to derive the free-free luminosity of each galaxy as:

$$L_{\nu}^{ff,ISM} = 3.2 \times 10^{-39} \frac{(1 - f_{esc})}{\alpha_B} \dot{N}_{ion} \text{ erg s}^{-1} \text{ Hz}^{-1}. \quad (6)$$

Once the galaxy emission properties and the value of f_{esc} are set as described in Section 2, the value of $L_{\nu}^{ff,ISM}$ is easily determined for every object. As the mode of star formation is directly related to the gas metallicity, we expect a change from massive Pop III to more standard Pop II stars once the metallicity is $Z \geq 10^{-4} Z_{\odot}$ (e.g.; Bromm et al. 2001; Schneider et al. 2001). This would result in a lower efficiency for production of ionizing photons. To roughly take this into account we assume that for $z < z_{ion}$, where $z_{ion} \sim 8$ (13) for the S5 (L20) case, the spectrum switches to a more standard one, typical of Pop II stars.

The emissivity from the more diffuse IGM HII regions can be directly derived from the reionization maps described in Section 2. From these, the value of n_e and the corresponding emissivity $\epsilon_{\nu}^{ff,IGM}$ are known for each cell of the simulation box. After reionization, $\epsilon_{\nu}^{ff,IGM}$ can be derived assuming that the ionization fraction in each cell is unity.

4.3 Galaxy Cluster Radio Halos and Relics

Diffuse, nonthermal radio emission extending over Mpc scales is a well established observational feature for a fair fraction of galaxy clusters. Diffuse radio sources are classified as either *radio halos* when their morphology is regular and typically centered on and resembling the X-ray emissivity; or as *radio relics* when they are irregular and located at the periphery of the cluster (in this case the radiation is typically polarized). In general the volume integrated emissivity is well characterized by a steep spectrum, $j(\nu) \propto \nu^{-\alpha}$ with $\alpha \geq 1$ (see e.g. Feretti 2002 for a review).

Statistically it is found that roughly 30 – 40% of rich galaxy clusters (X-ray luminosity $L_X \geq 10^{45} \text{ erg s}^{-1}$) do host a radio halo. In addition, it appears that the radio power (e.g. at 1.4 GHz) of radio halos scales steeply with the

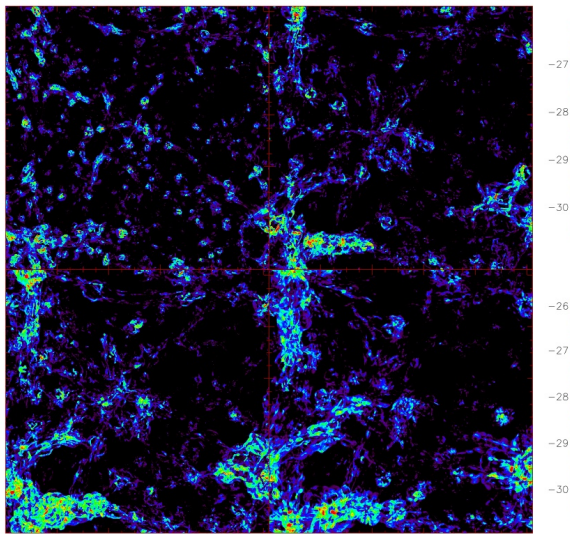


Figure 3. Maps of the synchrotron emission (at 150 MHz and in units of $\text{erg s}^{-1} \text{cm}^{-2} \text{Hz}^{-1} \text{arcmin}^{-2}$) from shock accelerated CR electrons, i.e. so called radio relics at redshift $z=3$ (top left), 1 (top right), 0.5 (bottom left) and 0 (bottom right). The map was obtained by adding the projections of the volume emissivity along the three coordinate axes. Thus, it is $50 h^{-1} \text{Mpc}$ on a side and $150 h^{-1} \text{Mpc}$ deep.

virial temperature of the associated clusters, i.e. $L_{1.4\text{GHz}} \propto T^\beta$ with $\beta \geq 4$ (Liang et al. 2000). The fraction drops below 10% when considering smaller clusters (i.e. $L_X \leq 10^{45} \text{ erg s}^{-1}$). It is generally believed, although still an open question, that this is mainly due to the limited sensitivity of current radio telescope (see, e.g., Liang et al. 2000; Bacchi et al. 2003)

The simulations described in Section 2 (Miniati et al. 2001) successfully reproduce most of the observed properties of radio halos and radio relics, particularly those relevant for the purpose of this paper. Thus, diffuse radio emission produced by synchrotron radiation from secondary e^\pm is characterized by a morphology and a low frequency radiation spectrum consistent with those of radio halos. In addition, the radio power (at 1.4GHz) scales with the cluster virial temperature with an index $\beta \sim 4.2$ which is consistent with the observations. Similarly, synchrotron emission from shock accelerated (primary) electrons is characterized by a spectrum, morphology and location that resemble closely those of radio relics.

For CR electrons with a distribution function $N(\gamma)$, such that $N(\gamma)d\gamma$ is the number of particles with Lorentz factor γ between γ and $\gamma + d\gamma$, the synchrotron emissivity (in units of $\text{erg cm}^{-3} \text{s}^{-1} \text{Hz}^{-1}$) is computed according to the expression (e.g. Rybicki & Lightman 1979)

$$\epsilon_\nu^{syn} = \frac{\sqrt{3}e^3 B}{m_e c^2} \sin \alpha \int_{\gamma_1}^{\gamma_2} F\left(\frac{2\nu\gamma^{-2}}{3\nu_B \sin \alpha}\right) N(\gamma) d\gamma, \quad (7)$$

where B is the magnetic field strength, α is the particles pitch angle (over which the ϵ_ν^{syn} is further averaged),

$\nu_B = eB/(2\pi m_e c)$, is the electron nonrelativistic gyrofrequency, $F(x) \equiv x \int_x^\infty dy K_{5/3}(y)$ with $K_{5/3}$ the modified Bessel function of order 5/3, and all other symbols have their usual meaning.

For the diffuse cluster radio halo emission, the population of CR electrons, $N(\gamma)$, is provided by secondary e^\pm . Consistently with current observational constraints, we consider that only 1/3 of galaxy clusters have radio halos, and further assume that radio halo formation is suppressed for objects of virial temperature below 1 keV. These two assumptions give us a fairly conservative estimate for this component.

For cluster radio relics, on the other hand, the emitting electrons, $N(\gamma)$, are those directly accelerated at cosmic shocks. Even though observations are sparser for radio relics than radio halos, we find that the radio power of the simulated relics is consistent with the values inferred from observations for a broad range of cluster temperatures (Miniati et al. 2001). In Fig. 3 we show four slices through the simulations of the emission from radio relics. We choose to show the maps for this component in particular to illustrate the complexity of its morphology. This will be important when discussing (in Sections 5.3 and 5.4) foreground removal.

5 ANGULAR CLUSTERING OF FOREGROUND FLUCTUATIONS

As we shall show in Section 5.4, the angular brightness temperature fluctuations due to foreground sources depend on two main quantities: the volume-average comoving emissivity and their projected two point correlation function. We will start by discussing these quantities for each of the foreground sources described above.

5.1 Comoving Emissivities

For the extended sources and point sources respectively the volume average comoving emissivity is simply given by,

$$\begin{aligned} \langle \epsilon_\nu(z) \rangle &= \frac{1}{V} \int_{extended} \epsilon_\nu(\mathbf{r}, z) dV \Big|_{L_\nu \leq L_\nu(S_c, z)} \\ &= \frac{1}{V} \sum_{point} L_\nu(z) \Big|_{L_\nu \leq L_\nu(S_c, z)} \end{aligned} \quad (8)$$

where V is the appropriate comoving simulation volume, $\epsilon_\nu(\mathbf{r}, z)$ in Eq. 8 is the emissivity at a given point in space, \mathbf{r} , and L_ν is the source luminosity which, for extended sources, is defined as $L_\nu = \int \epsilon_\nu dV_{eff}$ with the integral performed over the effective volume of the extended source (e.g. the cluster). The integration (summation) is performed over all points (sources) up to an emissivity (luminosity) corresponding to $L_\nu \leq L_\nu(S_c, z) \equiv S_c \times 4\pi d_L^2(z)$ where S_c is the flux cut off above which sources can be resolved and removed and d_L the luminosity distance (cf. Section 5.3).

In Fig. 4 we show the mean emissivity per comoving volume at the observed frequency $\nu = 115 \text{ MHz}$ as a function of redshift for radio galaxies (dotted line), ISM free-free emission (S5 run; long-short dashed line), IGM free-free emission (S5 run; short dashed line), cluster radio relics (long dashed line) and cluster radio halos (dashed-dotted line) as obtained

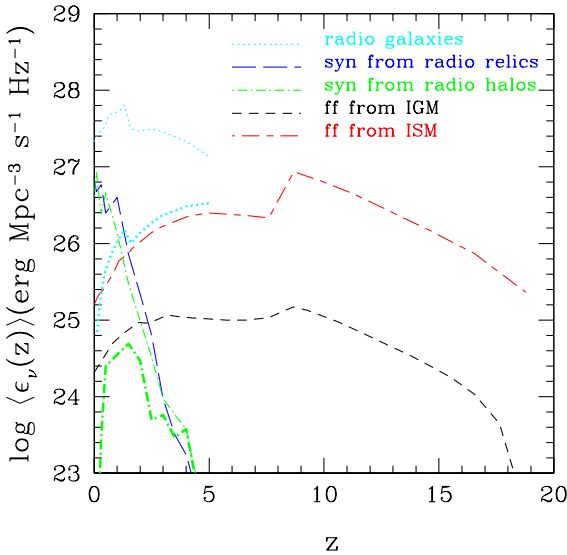


Figure 4. Redshift evolution of the mean comoving emissivity, at $\nu = 115$ MHz, due to: free-free from ISM HII regions (long-short dashed lines); free-free from IGM HII regions (short dashed lines) both in the S5 simulation; radio galaxies (thin dotted line and thick dotted line for $S_c = \infty$ and $S_c = 0.1$ mJy respectively); synchrotron from virialization shocks in radio relics (long dashed line); synchrotron from secondary electrons in radio halos generated in cosmic rays (thin and thick dash-dotted line for $S_c = \infty$ and $S_c = 0.1$ mJy respectively).

from the simulations. The thicker dotted and dash dotted lines show the emissivity when sources above $S_c = 0.1$ mJy have been removed. Here we will describe the total emissivities from the various components and reserve the discussion of source removal to Section 5.3.

As shown in Fig. 4, the radio galaxy, radio halos and relics were modeled in the simulation out to redshift $z = 5$, where most of the contribution is expected to come from. Below $z = 5$, the radio galaxy comoving emissivity dominates all the other components. Its peak, at $z \sim 2$, is attributed to the bright component of the luminosity function which is strongest around this redshift. However, the overall evolution of the radio galaxy $\langle \epsilon_\nu(z) \rangle$ is fairly flat. In contrast, for cluster radio halos and relics $\langle \epsilon_\nu(z) \rangle$ has a much steeper growth, by a factor $\gtrsim 10^4$, from $z = 5$ to $z = 0$. This is due to the rapid increase in the energy dissipated in shocks during merging/accretion events as a result of non-linear breaking of larger wave perturbations toward lower redshifts (Miniati et al. 2000). Finally, the free-free emission from ionized regions is significant only at high redshift, when the other contributions become negligible. The emissivity from IGM HII regions increases at $z < 20$, as ionization proceeds. Once it is completed, at $z \sim 8$ for the S5 case shown here, the emissivity decreases as the gas density decreases. The emissivity from ISM HII regions is instead proportional to the star formation rate. The drop observed in the curve is related to the drop in the ionizing photon production rate following reionization, as described in Section 4.2. This emissivity is consistent with the estimate

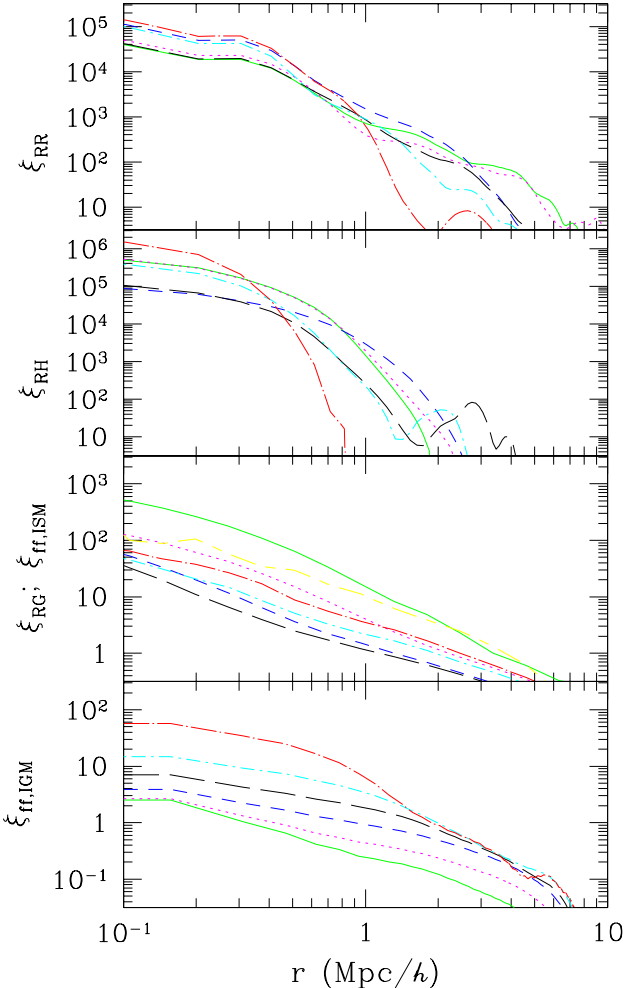


Figure 5. The spatial correlation functions $\xi(r, z)$ for cluster radio relics, halos, radio galaxies (and ISM free-free emission) and IGM free-free emission from top to bottom panel respectively. The spatial correlation functions are shown at $z = 0.1, 0.5, 1, 2, 3, 5$ (solid line, dotted, short dashed, long dashed, dot-short dashed, dot-long dashed) for radio halos and relics, at $z = 0, 1, 3, 5, 10, 13, 19$ (solid line, dotted, short dashed, long dashed, dot-short dashed, dot-long dashed) for the radio sources (and ISM free-free emission), and at $z = 13, 14, 15, 16, 17, 18$ for the free-free emission from the IGM (from bottom to top lines).

of Bianchi, Cristiani & Kim (2001), which is derived independently based on the observed star formation rate and a population synthesis model. In any case, the contribution from ISM HII regions is always greater than that from IGM HII regions, with the ratio reaching a maximum of ~ 700 at $z \sim 20$, when the IGM is mainly neutral, and a minimum of a few at lower redshift. In summary, we have shown that the radio galaxies, cluster radio relics and halos provide the largest contributions to the total comoving emissivity at moderate/low redshifts. The resulting brightness temperature fluctuations however, are also a function of the spatial clustering of the various components (described in Section 5.2).

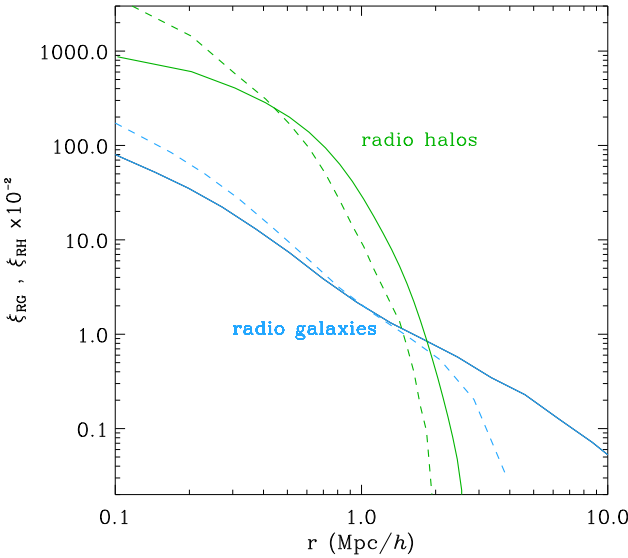


Figure 6. The spatial correlation function for radio galaxies and radio halos at $z = 2$ and $z = 1$ respectively. The solid lines show the correlation functions of the total sample, the dashes those for sources below the flux limit $S_c = 0.1$ mJy.

5.2 Spatial clustering

We quantify the spatial clustering of the various sources via the redshift dependent two-point correlation function, $\xi(r, z)$, defined as (Peebles 1993):

$$\xi(r, z) = \langle \delta(\mathbf{x}, z) \delta(\mathbf{x} + \mathbf{r}, z) \rangle, \quad (9)$$

where for extended sources, $\delta(\mathbf{x}, z) = \epsilon_\nu(\mathbf{x}, z) / \langle \epsilon_\nu(z) \rangle - 1$ and $\epsilon_\nu(\mathbf{x}, z)$ is the emissivity at a point with coordinate \mathbf{x} at redshift z . In practice, to evaluate $\xi(r, z)$ we have computed the power spectrum P_δ of $\delta(\mathbf{x}, z)$, and Fourier transformed:

$$\xi(r, z)_{\text{extended}} = \frac{1}{(2\pi)^3} \int P_\delta(k) \frac{\sin kr}{kr} 4\pi k^2 dk. \quad (10)$$

For the point source populations (radio galaxies and free-free emission from ISM) $\delta(\mathbf{x}, z) = n(\mathbf{x}, z) / \langle n(z) \rangle - 1$, where $n(\mathbf{x}, z)$ is number density of galaxies at \mathbf{x} . We evaluate the correlation function using the standard pair estimator,

$$\xi(r, z)_{\text{point}} = \frac{N(r, z)}{N_{\text{random}}(r, z)} - 1, \quad (11)$$

where $N(r, z)$ is the number of pairs separated by a distance r , and $N_{\text{random}}(r, z)$ is the number of pairs in the same r -bin expected if galaxies were randomly distributed. Because our simulated box is not periodic, we generate random catalogues to compute $N_{\text{random}}(r, z)$. From top to bottom, Fig. 5 shows the computed $\xi(r, z)$ for the cluster radio relics, ξ_{RR} , halos, ξ_{RH} , radio galaxies, ξ_{RG} , (the same as free-free emission from ISM, $\xi_{ff,ISM}$ as they are the same halos) and free-free emission from IGM, $\xi_{ff,IGM}$ (see caption of Fig. 5 for details). According to our model, the radio galaxies constitute a random sample of all halos (the duty cycle is not mass dependent, c.f. Section 4.1). As we expect, the correlation function of the galaxy population is close to a power law of the form $\xi(r) \sim (r/r_0)^{-\gamma}$ (usually slightly suppressed on scales $r \lesssim 20 - 50$ kpc) and with a correlation length,

r_0 which varies in the range of $r_0 \sim 2 - 5 h^{-1}$ Mpc in the redshift range studied (Fig. 5). Note that the amplitude of the correlation function grows with decreasing redshift for $z \lesssim 10$. At higher redshift the trend is reversed probably as an effect of the mass resolution (when halos of mass corresponding to the resolution limit start representing the high end tail of the mass function). This is not important as all of the signal from point sources is dominated by relative low redshifts (c.f.; Section 5.4).

The correlation functions for radio halos and radio relics have typically large amplitudes, a rather flat inner region and a steep decline at $r \gtrsim 1 h^{-1}$ Mpc (particularly in the case of radio halos). The correlation length for cluster radio halos is set predominantly by the size itself of the brightest sources, which is roughly of order of a Mpc or so. Radio relics are typically more extended, as reflected also by their correlation functions, which decline less steeply than in the case of radio halos. This is a consequence of the fact that accretion shocks can cover larger regions than that of the cluster, particularly when two or more groups/clusters are approaching before a merger (see Fig. 3).

Finally, for the correlation functions of the IGM free-free emission we only show those corresponding to $z > z_{\text{ion}}$. We note that as ionization proceeds the HII regions, which initially are isolated and surrounding the galaxies, will become increasingly more extended and, as expected, will start overlapping. This has the consequence that the correlation amplitude decreases with decreasing redshifts. Because the IGM free-free emissivity shown in Section 5.1 and its correlation function are negligible with respect to the other components (and in particular with respect to free-free emission from the ISM) we will not consider it further.

5.3 Bright source removal

As part of the actual experiment, bright enough sources will be directly identified as foreground contaminants, and hence removed from the observational maps without contributing to the brightness temperature fluctuations. The flux limit above which sources can be removed, S_c , will of course be dependent on the instrument sensitivity. Here we take $S_c = 0.1$ mJy, corresponding to the expected sensitivity for source detection by LOFAR and discuss the major effects that this has on both the emissivities and correlations functions.

Note that removal of point sources will be far easier than the removal of extended components. Here we shall illustrate the effects of applying a flux cut on radio galaxies and on cluster radio halos (because, as we shall show in Section 5.4, these are the two dominant contaminants of each class). For cluster radio halos, we go back to the volume emissivity distribution calculated from the simulation and calculate the total radio luminosity of each identified cluster by integrating the synchrotron emissivity over its volume (roughly out to the virial radius, r_{vir}), $L_\nu = \int_0^{r_{\text{vir}}} \epsilon_\nu 4\pi r^2 dr$. The cluster radio emission is then removed from the volume emissivity distribution if $L_\nu \geq S_c \times 4\pi d_L^2$. As shown by Fig. 3 and discussed in Section 4.3 the morphology of radio relics is fairly complex. We will not attempt here to remove this extended component. However, we do expect it to provide similar advantages as those gained from the removal of cluster radio halos which we describe below. Nevertheless, such an oper-

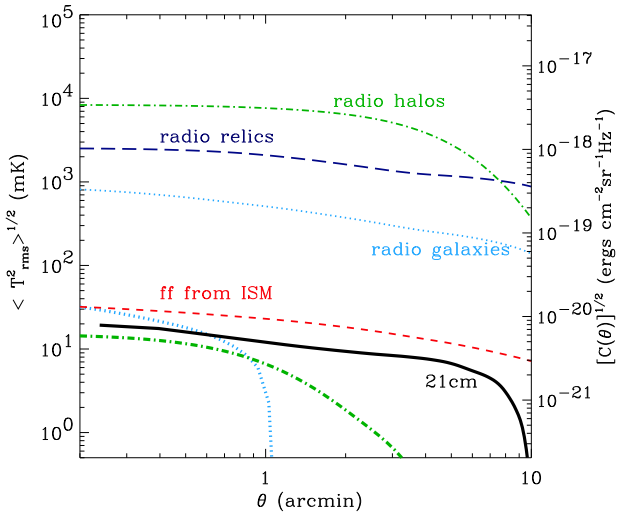


Figure 7. Prediction for the correlation signal owing to intensity fluctuations of radio galaxies (dotted lines), ISM free-free emission (short dashed), radio relics (dashed dotted), radio halos (long dashed) at $\nu = 115$ MHz. The thicker lines show the signal when sources above a flux $S_c = 0.1$ mJy are removed. The solid line shows the primary correlation signal due to the redshifted 21cm

ation for cluster radio relics may turn out more difficult due to their more irregular morphology.

As shown in Fig. 4, the removal of sources above the detection threshold has the obvious effect of decreasing the volume emissivity (c.f; Eq. 8). Because of the relatively low flux cut level the emissivity drops dramatically towards the low redshifts. In particular, for radio galaxies emissivity decreases between a factor of ~ 10 to ~ 200 from $z = 5$ to $z = 0.1$ with respect to the case when no sources have been removed. For radio halos removal of sources above $S_c = 0.1$ mJy significantly affects the emissivity below $z \sim 2$. At $z < 2$ the emissivity decreases by up to a factor of a few thousand.

In addition to affecting the overall emissivity, the removal of bright sources has an important effect on the spatial correlation functions. As an illustrative example, we show in Fig. 6 the correlation function for radio galaxies and radio halos at $z = 2$ and $z = 1$ respectively (solid lines) compared with the case in which a flux cut, $S_c = 0.1$ mJy is applied (dashed lines), and all the objects with flux exceeding S_c have been removed from the respective simulated catalogues. Typically, removing the bright sources has the effect of steepening the spatial correlation function and hence decreasing the correlation lengths. In particular, for the radio galaxies, the amplitude at scales $r \lesssim 1h^{-1}\text{Mpc}$ is boosted, but at scales larger than the typical correlation length it is significantly suppressed. For the case of radio halos, the effect is similar and the suppression of the correlation functions occurs at even smaller scales than in radio galaxies. Also, because the correlation functions of these sources decline very steeply the overall effect is more dramatic at large scales.

For the radio galaxies, we see from Fig. 6 that the correlation function of objects below a flux cut is biased in a scale dependent way with respect to the whole population. This is very different to the alternate case of galaxies brighter than flux S_c . For the latter, we find that the correlation function of the brightest galaxies is similar in shape to that of the whole population (linear biasing), even on scales significantly smaller than the correlation length (as found by e.g., Mo & White 1996). Note that we have checked that the effects we have just described, scale dependent bias versus linear bias, are the same when a mass cut is adopted instead of a flux cut. We have checked this by calculating the correlation function ξ for objects below and above a given dark mass limit M_{min} . This is expected as in our model we have directly linked e.g., the radio galaxy population to the dark matter potential. The relative change in clustering of halos after applying an upper mass threshold is not often considered, but the boost in clustering on small scales which results, along with suppression on linear scales, is expected in hierarchical models of structure formation (e.g. Sheth & Tormen 1999).

Finally, we note that, as we shall show in the next Section, the dependence of the spatial clustering on the flux cutoff is important when the spatial functions are mapped into the angular clustering signal. Such an effect had not been taken into account previously in calculations of sky intensity fluctuations due to clustering of foreground sources within the context of the 21cm experiment.

5.4 Angular Clustering

We now calculate the contribution to the intensity fluctuations, δI , owing to the inhomogeneities in the space distribution of the various sources described above. The angular correlation function of such intensity fluctuations is given by,

$$C(\theta) = \langle \delta I(\phi) \delta I(\phi + \theta) \rangle, \quad (12)$$

where ϕ, θ are angular coordinates, and $\delta I(\phi) = [I(\phi)/\langle I \rangle] - 1$, where $I(\phi)$ is the intensity at angular position ϕ .

Following the standard approach, we use the Limber projection (Limber 1953; Peebles 1993) to calculate, $C(\theta)$ (in units of $\text{erg}^2 \text{ s}^{-2} \text{ cm}^{-4} \text{ Hz}^{-2} \text{ sr}^{-2}$):

$$C(\theta) = \frac{1}{(4\pi)^2} \int_0^\infty dV_1 dV_2 \frac{\langle \epsilon_\nu(z_1) \rangle}{4\pi d_L^2(z_1)} \frac{\langle \epsilon_\nu(z_2) \rangle}{4\pi d_L^2(z_2)} \xi(r, z_1, z_2), \quad (13)$$

where $dV_1, dV_2, \langle \epsilon_\nu(z_1) \rangle, \langle \epsilon_\nu(z_2) \rangle$ are the comoving volumes and emissivities at redshifts z_1 and z_2 respectively. For small angles θ and small radial distances, $z_1 \sim z_2 \sim z$ and we write:

$$C(\theta) = \frac{1}{(4\pi)^2} \int_{z_{min}}^{z_{max}} dz \frac{\langle \epsilon_\nu(z) \rangle^2}{(1+z)^2} \frac{dx}{dz} \int_{u_{min}}^{u_{max}} du \xi(r, z), \quad (14)$$

where $\xi(r, z)$ is the spatial two point correlation function, $r^2 = u^2 + x^2 \theta^2$, and x is the comoving coordinate, related to the redshift (for the flat models) by:

$$x = \frac{c}{H_0} \int_0^z [\Omega_0(1+z')^3 + \Omega_\Lambda]^{-0.5} dz', \quad (15)$$

and we have written $dz_1 dz_2 = (dz/dx) du dz$ for $x_1 \sim x_2 \sim x$ in Eq. 13. Analogously, using the standard Limber

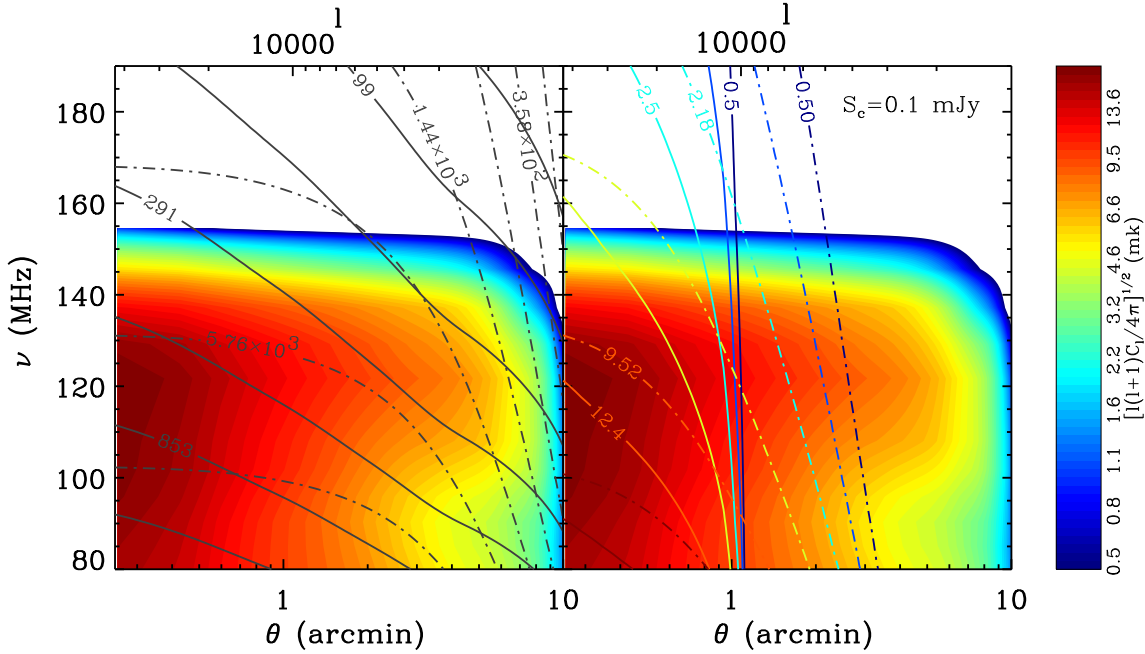


Figure 8. Contours of the angular power spectrum (in mK) of the the 21cm fluctuations (shaded area) and the angular power spectra due to intensity fluctuations of radio galaxies (solid contours) and radio halos (dot-dashed contours) as a function of angle (l) and observed frequency. The lines in the right panel show the contours for the total foreground signals. In the left panel, foreground sources below a flux limit $S_c \gtrsim 0.1$ mJy have been removed.

equation the angular correlation function, $w(\theta)$ (c.f., Eq. 4), can be written as,

$$w(\theta) = \int_{z_{min}}^{z_{max}} \int_{u_{min}}^{u_{max}} du dz \frac{dz}{dx} \xi(r, z). \quad (16)$$

We can then simply rewrite the angular clustering of intensity fluctuations in terms of a brightness temperature fluctuation in the sky as:

$$\langle T_{rms}^2 \rangle^{1/2} = \left[\frac{l(l+1)C_l}{4\pi} \right]^{1/2} \left(\frac{\partial B_\nu}{\partial T} \right)^{-1}, \quad (17)$$

where,

$$\frac{\partial B_\nu}{\partial T} = \frac{2k}{c^2} \left(\frac{kT}{h} \right)^2 \frac{x^4 e^x}{(e^x - 1)^2}, \quad (18)$$

with $x = h\nu/kT$ and $T = 2.725$ K. The power spectrum, C_l (in units of $\text{erg}^2 \text{s}^{-2} \text{cm}^{-4} \text{Hz}^{-2} \text{sr}^{-1}$), is related to $C(\theta)$ by the Legendre transform as:

$$C_l = 2\pi \int d(\cos\theta) P_l(\cos\theta) C(\theta) \sim 2\pi \int_0^\infty d\theta \theta J_0(l\theta) C(\theta), \quad (19)$$

where J_0 is the Bessel function and the last step is valid for $l \gg 1$. Fig. 7 shows the prediction for the correlation signal caused by the intensity fluctuation due to radio galaxies (dotted lines), ISM free-free emission (short dashed), cluster radio relics (dashed dotted), cluster radio halos (long dashed) at $\nu = 115$ MHz, the frequency at which the 21cm emission peaks, according to S5 model of CM. The thinner

lines show the total signal when no flux cutoff has been applied, while the thicker lines show the signal when sources above a flux $S_c = 0.1$ mJy (corresponding to the planned detection limit of LOFAR) are removed. The solid line shows the primary correlation signal due to the redshifted 21cm emission. The total T_{rms} signal due to any of the foreground components exceeds the primary 21cm signal. In particular, the extended sources such as the radio halos and radio relics provide fluctuations about three (and more) orders of magnitude and the radio galaxies about two orders of magnitude larger than the 21cm emission through the whole range of angular scales. The rms fluctuations due to free-free emission from the ISM, instead, are close to those of the 21cm. However, the effective brightness temperature fluctuations due to foreground sources after the removal of sources with $S > S_c$ (for illustration we have applied the removal only to the highest point and extended components of the rms fluctuations, e.g. radio halos, and radio galaxies), decrease significantly. For the radio galaxies, detection and removal of sources above $S_c = 0.1$ mJy decreases the fluctuations due to this component down to the level of the 21cm emission at scales $\theta \lesssim 1$ arcmin. Above these angular scales the foreground signal drops out completely. This is a result of the combined effects of the decrease of the overall emissivity (e.g., Fig. 4) and the suppression of the the amplitude of spatial correlation of faint radio sources at the scales that map into angular scales of $\theta \gtrsim 1$ arcmin (where radial scales and angular scales are roughly related as, $r \sim 3(\theta/1')[(1+z)/1]^{0.2} h^{-1}$ Mpc). For this flux cut, an-

angular scales of $\theta \gtrsim 1$ arcmin are thus free of this contaminating signal, rendering the 21cm tomography free of the radio galaxy contamination. A similar result is obtained when the flux cut is applied to the radio halos. The decrease in amplitude in this rms fluctuation is even more pronounced than in the case of radio galaxies. The signal drops to the level of the primary 21cm at $\theta \lesssim 1$ arcmin and is also well below it at larger angular scales. Applying the same flux cut to the ISM free-free emission sources, would lead to a similar effect as for the radio galaxies, but in this case, the signal would drop well below that of the 21cm on all scales (and below the axis range plotted in Fig 7).

After removing sources with flux above $S_c = 0.1$ mJy, the dominant contribution to the rms fluctuations from radio halos comes from $0.6 \lesssim z \lesssim 2$. Similarly for the case of the radio sources (which however show a different evolution of their mean emissivity and different clustering), the main contribution to the rms fluctuations is in the range $0.5 \lesssim z \lesssim 2.5$. This is set by the the projection of the emissivity and correlation function as shown in Eq. 14.

6 CONCLUSIONS

We have examined the contribution of extragalactic foregrounds to the angular brightness temperature fluctuations at the frequencies relevant for observations of the redshifted 21cm signal. We have used a set of cosmological simulations to model the evolution of radio galaxies, free-free emission from the ISM and IGM and radio halos and relics. We calculated their comoving space density emissivity and spatial correlation functions and projected the simulation volumes to predict their expected sky temperature fluctuations.

Because high resolution observations of the 21cm signal will be carried out in both frequency and angle it is best to summarize the main conclusion from our analysis by showing the intrinsic and foreground signals as a function of both scale and frequency. Fig. 8 shows the angular power spectrum of the 21cm signal (from CM simulations), and that of the radio galaxies and radio halos (the two dominating foreground components for which source removal was studied here) as a function of frequency (where we have taken the spectral index of radio galaxies and radio halos to be $\alpha = 0.8$ and 1 respectively) and angle (scale l). In summary,

- As previously emphasized by Di Matteo et al. (2002, for the case of radio galaxies) and Oh & Mack (2002, for the case of free-free emission from the ISM) we have found that the absolute foreground signal fluctuates more strongly than that of the 21 cm signal at all angular scales and frequencies (left panel Fig. 8). In addition, here we have shown that the largest fraction of these fluctuations is due to extended cluster radio halos and relics, both of which had previously been neglected. Radio emission from the cores of galaxies contributes more strongly than the free-free emission from their ISM. The presence of foreground signal many orders of magnitude above the primary signal needs to be addressed because it may seriously hinder the detection of the 21 cm line emission as the latter could be easily mimicked by small errors/irregularities in the subtraction of the foreground spectra.

- We have considered source removal above a flux limit $S_c = 0.1$ mJy, (close to LOFAR sensitivity) for point sources

and radio halos (as an example of an extended source). We have found that, as expected, the amplitude of the foreground power spectra of both radio halo and radio galaxies decreases at all scales. In particular, with the additional spatial information on the foreground sources provided by the simulations, we have shown that the amplitude of the angular foreground fluctuations drops well below that of the 21cm at scales $\theta \gtrsim 1$ arcmin and becomes comparable to it at scales smaller than $\theta \sim 1$ arcmin (right panel Fig. 8). At angular scales larger than $\theta \sim 1$ arcmin and at frequencies $\nu \lesssim 150$ MHz (simply corresponding to the redshifts prior to full reionization in the S5 model) the 21cm signal should be detected directly. At scales smaller than $\theta \sim 1$ arcmin, subtraction of the foregrounds can be feasibly carried out in frequency space, as the overall foreground signal is at most of the same order as the primary 21cm. Comparing maps closely spaced in frequency, (as discussed in detail by Zaldarriaga et al. 2004) after the removal of bright sources should make the detection of the signal feasible at small scales also (where the foreground power spectra are different than the one of the 21 cm; Fig. 8)¶.

From Fig. 8, we conclude that bright sources contribute to the angular power spectrum at $\theta \gtrsim 1$ arcmin and, once removed, the power on these scales is suppressed. This effect is due to a scale dependent bias of the spatial correlation functions of sources below a certain flux cut. This result emphasizes the importance, when determining the angular fluctuation and power spectra of foregrounds, of using simulations to project the detailed spatial distribution of foregrounds as a function of flux cut. Analytical estimates of brightness temperature fluctuations (Di Matteo et al. 2001; Oh & Mack 2002), which had to assume a certain angular clustering of the radio foregrounds, appear to be insufficient for determining the effect of these contaminants on all scales. This had lead previous authors to generally more pessimistic conclusions for the feasibility of 21cm tomography. We find instead that, due to the effects of bright source removal, 21cm observations carried out at angular scales θ of the order of a few arcmin should not be strongly affected by extragalactic foregrounds. However, how source subtraction can be carried out from the observed maps, needs detailed work. The maps we have simulated will need to be folded with the instrument response functions as a function of angle and frequency (and other specific details of the instrument design). This is currently being investigated for the case of LOFAR by Valdes et al. (2004).

We note that determining the angular scale at which the foreground signal should drop out is, of course, subject to some uncertainty associated to specifics of source removal. Besides needing to account for the instrument response, which is beyond the scope of this paper, this will of course be a function of the theoretical approach we have adopted to model the foreground source populations down to flux limits currently unobserved. In fact, it is part of the

¶ We note further that the amplitude of the 21cm signal shown in Fig. 8 corresponds to a given bandwidth $\Delta\nu = \nu\Delta z/(1+z) = 1\text{MHz}$ and is expected to increase with bandwidth resolution. CM show that the signal can increase by a factor up to 4 at small angles and high frequencies if e.g.; $\Delta\nu = 0.1\text{MHz}$ can be achieved making foreground subtraction less crucial at scales $\theta \lesssim 1'$

scientific goals of future high sensitivity low frequency radio facilities such as LOFAR, PAST and SKA to sample for the first time faint radio galaxies and diffuse cluster radio emission (radio halos and radio relics, see Enßlin & Röttgering 2002, Brüggen et al. 2004) and hence determine the properties of these population up to high redshifts.

ACKNOWLEDGMENTS

We would like to thank F. Stoehr for providing us with his simulations, S. Bertone for the fof catalogues, R. Croft, H. Röttgering, J. Peterson, S. Bianchi, A. Diaferio and M. Magliocchetti for many useful discussions. The paper has been partially supported by the Research and Training Network “The Physics of the Intergalactic Medium” set up by the European Community under the contract HPRN-CT-2000-00126.

REFERENCES

Bacchi, M., Feretti, L., Giovannini, G. & Govoni, F. 2003, *A&A*, 400, 465

Baes, M., Buyle, P., Hau, G.K.T. & Dejonghe, H. 2004, *MNRAS*, in press (astro-ph/0303628)

Becker, R. H. et al. 2001, *AJ*, 122, 2850

Bell, A. R. 1978, *MNRAS*, 182, 147

Bianchi, S., Cristiani, S. & Kim, T.-S. 2001, *A&A*, 376, 1

Bromm, V., Ferrara, A., Coppi, P.S. & Larson, R.B. 2001, *MNRAS*, 328, 969

Brüggen, M., Enßlin, T. A., Miniati, F. 2004, *ApJ*, submitted, e-print astro-ph/0309612

Carilli, C., Gnedin, N. Y. & Owen, F. 2002, *ApJ*, 577, 22

Cavaliere, A., Vittorini V., 2002, *ApJ*, 570, 114

Chen, X. & Miralda-Escudé, J. 2003, astro-ph/0303395

Ciardi, B., Ferrara, A., Marri, S. & Raimondo, G. 2001, *MNRAS*, 324, 381

Ciardi, B., Ferrara, A. & White, S.D.M. 2003, *MNRAS*, 344, L7 (CFW)

Ciardi, B. & Madau, P. 2003, *ApJ*, 596, 1 (CM)

Ciardi, B., Stoehr, F. & White, S.D.M. 2003, *MNRAS*, 343, 1101 (CSW)

Ciotti, L. & van Albada, T.S. 2001, *ApJ*, 552, L13

Di Matteo, T., Croft, R.A.C., Springel, V. & Hernquist, L. 2003a, *ApJ*, 593, 56

Di Matteo, T., Croft, R.A.C., Springel, V., & Hernquist, L. 2003b, *ApJ*, submitted

Di Matteo, T., Perna, R., Abel, T. & Rees, M. J. 2002, *ApJ*, 564, 576

Dunlop, J.S., Peacock, J.A. 1990, *MNRAS*, 247, 19

Enßlin, T. A., Röttgering, H. 2002, *A&A*, 396, 83

Elvis, M., Risaliti, G., Zamorani, G. 2002, *ApJ*, 565, L75

Elvis, et al. 1994, *ApJS*, 95, 1

Falcke, H., Koerding, E. & Markoff, S. 2003, *A&A*, in press (astro-ph/0305335)

Fan, X. et al. 2001, *AJ*, 122, 2833

Fan, X. et al. 2003, *AJ*, 125, 1649

Ferrarese, L. 2002, *ApJ*, 578, 90

Ferrarese L. & Merritt D., 2000, *ApJ*, 539, L9

Feretti, 2002, in ‘The Universe at Low Radio Frequencies’, Proceedings of IAU Symposium 199, Pune, India, Edited by A. Pramesh Rao, G. Swarup, and Gopal-Krishna, p.133

Field, G. B. 1958, *Proc. IRE*, 46, 240

Field, G. B. 1959, *ApJ*, 129, 551

Furlanetto, S., & Loeb, A. 2002, *ApJ*, 579, 1

Furlanetto, S., Sokasian, A. & Hernquist, L. 2004, *MNRAS*, 347, 187

Gebhardt K. et al. 2000, *ApJ*, 539, L13

Gnedin, N.Y. & Shaver, P.A. 2003, *ApJ*, submitted (astro-ph/0312005)

Gunn, J.E. & Peterson, B.A. 1965, *ApJ*, 142, 1633

Haiman Z., Ciotti L., Ostriker J.P., 2003, *ApJ*, submitted [astro-ph/0304129]

Iliev, I. T., Shapiro, P. R., Ferrara, A., & Martel, H. 2002, *ApJ*, 572, L123

Iliev, I. T., Scannapieco, E., Martel, H., & Shapiro, P. R. 2003, *MNRAS*, 341, 81

Kang, H. & Jones, T. W. 1995, *ApJ*, 447, 994

Kauffmann, G., Colberg, J. M., Diaferio, A. & White, S. D. M. 1999, *MNRAS*, 303, 188

Kauffmann G., Haehnelt M., 2000, *MNRAS*, 311, 576

Kogut, A. et al. 2003, *ApJS*, 148, 161

Kumar, A., Padmanabhan, T., Subramanian, K., 1995, *MNRAS*, 272, 544

Liang, H., Hunstead, R. W., Birkinshaw, M., & Andreani, P. 2000, *ApJ*, 544, 686

Limber, D., 1954, *ApJ*, 119, 655

Madau, P., Meiksin, A., & Rees, M. J. 1997, *ApJ*, 475, 492

Magliocchetti M., Maddox M., Lahav O., & Wall J., 1998, *MNRAS*, 300, 257

Maselli, A., Ferrara, A. & Ciardi, B. 2003, *MNRAS*, 345, 379

Merloni A., Heinz S., Di Matteo T., 2003, *MNRAS*, 345, 1057

Miniati, F., Ryu, D., Kang, H., Jones, T. W., Cen, R. & Ostriker, J. P 2000, *ApJ*, 542, 608

Miniati, F., Jones, T. W., Kang, H., & Ryu, D. 2001, *ApJ*,

Miniati, F. 2001, *Comp. Phys. Comm.*, 141, 17

Miniati, F. 2002, *MNRAS*, 337, 199 562, 233

Mo, H.J. & White, S.D.M. 1996, *MNRAS* 282 347

Monaco, P., Salucci P., & Danese L., 2000, *MNRAS*, 311, 279

Oh, S. P. 1999, *ApJ*, 527, 16

Oh, S. P. & Mack, K. J. 2003, *MNRAS*, 346, 871

Overzier R.A., Röttgering H.J.A., Regenlink R.B., Wilman R.J., 2003, *A&A*, 405, 53

Peebles, P. J. E. 1993, *Principles of Physical Cosmology* (Princeton New Jersey: Princeton University Press)

Pentericci et al. 2002, *ApJ*, 123, 2151

Richards E.A., 2000, *ApJ*, 533, 611

Rybicki, G.B. & Lightman, A.P. 1979, *Radiative Processes in Astrophysics* (New York: Wiley)

Ryu, D., Ostriker, J. P., Kang, H., & Cen, R. 1993, *ApJ*, 414, 1

Schneider, R., Ferrara, A., Natarajan, P. & Omukai, K. 2002, *ApJ*, 571, 30

Scott, D., & Rees, M. J. 1990, *MNRAS*, 247, 510

Shaver, P., Windhorst, R., Madau, P. & de Bruyn, G. 1999, *A&A*, 345, 380

Sheth, R., & Tormen, G., *MNRAS* 308, 119

Spergel, D.N. et al. 2003, *ApJS*, 148, 175

Springel, V., White, S. D. M., Tormen, G. & Kauffmann, G. 2001, *MNRAS*, 328, 726 (SWTK)

Springel, V., Yoshida, N. & White, S. D. M. 2001, *NewA*, 6, 79

Tozzi, P., Madau, P., Meiksin, A. & Rees, M.J. 2000, *ApJ*, 528, 597

Tremaine S. et al., 2002, *ApJ*, 574, 554

Valdes et al, 2004, in preparation

Volonteri M., Haardt F., Madau P., 2003, *ApJ*, 582, 559

Willott C.J., Rawlings S., Blundell K.M., Lacy M., Eales S.A., 2001, 322, 536

Wilman R.J., Röttgering H.J.A., Overzier R.A., Jarvis M.J., 2003, *MNRAS*, 399, 695

White, R. L., Becker, R. H., Fan, X. & Strauss, M. A. 2003, *AJ*, 126, 1

Wyithe J.S., Loeb A., 2002, *ApJ*, 581, 886

Yoshida, N., Sheth, R. K. & Diaferio, A. 2001, *MNRAS*, 328, 669

Zaldarriaga, M., Furlanetto, S. & Hernquist, L. 2004, ApJ, submitted (astro-ph/0311514)